International Journal of Biological Macromolecules 199 (2022) 275–286

Contents lists available at ScienceDirect

International Journal of Biological Macromolecules

journal homepage: www.elsevier.com/locate/ijbiomac

An interference-free new xanthine biosensor based on immobilized enzyme-nanogold conjugate on carbon nanotube doped poly (3,4-Ethylenedioxythiophene) composite film

Sarani Sen [a,b,*], Priyabrata Sarkar [a,c]

[a] Department of Polymer Science and Technology, University of Calcutta, 92 APC Road, Kolkata 700009, India
[b] Calcutta Institute of Pharmaceutical Technology and Allied Health Sciences, Banitabla, Uluberia, Howrah 711316, India
[c] Calcutta Institute of Technology, Banitabla, Uluberia, Howrah 711316, India

ARTICLE INFO

Keywords:
Xanthine oxidoreductase
Gene cloning
Differential pulse voltammetry
Polymeric nanobiocomposite. Biosynthesized gold nanoparticles
Electrochemical biosensor

ABSTRACT

A new design of biosensor based on polymeric nano(bio)composite has been proposed for the selective detection of xanthine to be used in the clinical analysis as well as food quality control. The xanthine oxidoreductase (XOR) gene of *Pseudomonas aerogenosa* strain CEBP1 was cloned to obtain purified enzyme through affinity chromatography. fMWCNT doped PEDOT was electrodeposited on the working electrode to enhance the sensitivity and selectivity of the biosensor. Bio-synthesized gold nanoparticles conjugated XOR (Au-XOR) was covalently immobilized on the polymeric nanocomposite. The enzymatic activity was enhanced 1.12 times with increased substrate affinity. The surface morphology and structural properties of the polymeric layer were investigated using SEM, FESEM, TEM. Electrochemical characteristics were performed by cyclic voltammetry, differential pulse voltammetry (DPV), and electrochemical impedance spectroscopy. Xanthine was oxidized (pH 7.0) on the uniquely designed polymeric nano(bio)composite modified electrode at a lower anodic potential of + 0.446 V vs. Ag/AgCl (3 M NaCl) at optimized DPV conditions. The simple, newly designed Au-XOR/fMWCNT-PEDOT/GCE exhibited interference-free reproducibility and stability (~4 months) with excellent sensitivity of 16.075 μA.μ M^{-1}.cm^{-2} for the quantification of xanthine in biological samples such as blood, tissue, urine. The applicability of the biosensor was validated by comparing the sensing results for the real biological fluidic solutions with HPLC data (RE = 0.5–3.1%).

1. Introduction

Xanthine (XN) is an important bioanalyte for biomedical and food processing industries [1]. XN is an evaluating index for monitoring the freshness of fish, meat, and other protein-derived products as it starts to accumulate right after the animal is slaughtered due to microbial degradation of ATP following the pathway ATP → ADP → AMP → IMP → HxP → HX → XN [2–5]. XN is the first indicator of an abnormal purine profile, as it is the metabolic precursor of uric acid. The generated reactive oxygen species (ROS) in this process are also involved in numerous vital biological downstream processes. Thus abnormalities in the purine degradation pathway may cause various clinical disorders, including perinatal asphyxia, adult respiratory distress syndrome, cerebral ischemia, tumor, hyperthermia, and pre-eclampsia [6–8]. Extreme abnormal levels of XN in body fluids are symptoms of several diseases, such as renal failure, hyperuricemia, gout, xanthinuria, leukemia, and pneumonia [5,7].

Xanthine oxidoreductase (XOR) is a prime enzyme that oxidizes hypoxanthine to xanthine and xanthine to uric acid [3,8,9]. XOR is a homodimeric cytosolic molybdenum protein with a molecular mass of around 290 kDa [8,9]. Each subunit acts independently during the oxidation process, having two distinct iron-sulfur ([2Fe-2S]) centers, one molybdopterin (Mo) cofactor, and one flavin adenine dinucleotides (FAD) [8–10]. Mo(VI) transforms to its reduced form Mo(IV) during the oxidative hydroxylation process. Two generated electrons pass successively through [2Fe-2S] centers to FAD, and finally to molecular oxygen (O_2) [7–10]. Reactive oxygen species (ROS) such as superoxide radical ($O_2^{\bullet-}$) and hydrogen peroxide (H_2O_2) are produced at the end of the oxidative reaction [8].

It was noted from our previous study that *Pseudomonas aerogenosa*

* Corresponding author at: Assistant Professor, Calcutta Institute of Pharmaceutical Technology and AHS, Banitabla, Uluberia, Howrah.
E-mail addresses: sspst_rs@caluniv.ac.in (S. Sen), principal.cit@urschard.in (P. Sarkar).

https://doi.org/10.1016/j.ijbiomac.2021.12.094
Received 30 April 2021; Received in revised form 30 November 2021; Accepted 16 December 2021
Available online 5 January 2022

strain CEBP1 exhibited the highest XOR activity in comparison to other isolated strains when it was incubated in selective xanthine media (SXM) at optimized conditions [11]. In the present research work, the XOR gene of P. sp. CEBP1 was expressed in *E.coli* BL21 and recombinant XOR enzyme was purified for sensor fabrication. Since XOR is an intracellular enzyme, after bacterial cell disruption for extraction of XOR, the cell-free extracellular extract (CFE) was used for biosynthesis of gold nanoparticles (Au NP). This study aimed to utilize the AuNP for enhanced activity of XN oxidizing enzyme, and eventually further enhancement of the stability of the biosensing platform. This Biosynthesised AuNP was conjugated with purified XOR enzyme (Au-XOR) and the interaction of AuNP with XOR was studied by various spectrophotometric techniques such as UV–vis, fluorescence, circular dichroism (CD). The proposed technique can be applied for the economical production of purified XOR enzyme to be used in biomedical applications.

Green synthesized nanoparticles such as gold (Au), silver (Ag), platinum (Pt) have immense importance in modern science [12–14]. The non-toxic and cost-effective biosynthesized nanoparticles could be isolated from various microbes and, plant sources [12,15,16]. Gold NP has been widely used in biomedical applications due to its antibacterial, anticancer, imaging, and conducting nature. AuNP provides a suitable microenvironment to retain the biological activity of proteins upon adsorption and enhance storage stability [17,18]. It has an attractive role in the fabrication of biosensing matrix because of its unique properties such as large effective surface area, excellent electron transfer, fast mass transport rate, and good biocompatibility [2,17,19–21]. In the last two decades, different materials such as metal nanomaterials (Au, Ag, Pt, Cu, ZnO, Fe_3O_4), carbon (e.g. nanotube, graphene, nanofiber, nanohorn), self-assembled monolayers, conducting and nonconducting polymers have widely been incorporated to enhance the electron transfer rate of enzyme electrodes, that further helps to increase the sensitivity of biosensor [2,17,19–24]. Carbon nanotubes and conducting polymers both offer excellent biocompatibility as well as catalytic activities [2,4,7,17,19,22,24–26]. In this work, we have synthesized a uniform thin film of functionalized multiwalled carbon nanotube (fMWCNTs) doped poly(3,4-ethylenedioxythiophene) (PEDOT) through a rapid one-step electropolymerization process for immobilization of nanogold conjugated purified XOR (Au-XOR) to fabricate an enzyme-based biosensing matrix.

2. Experimental

2.1. Chemicals

3,4 ethylenedioxythiophene (EDOT), auric chloride ($HAuCl_4{\cdot}3H_2O$), and multiwalled carbon nanotube (MWCNT) were supplied by Sigma (US). Potassium nitrate, potassium dihydrogen phosphate (KH_2PO_4) and dipotassium hydrogen phosphate (K_2HPO_4), sodium chloride (NaCl), peptone, beef extract, yeast extract, agar-agar were purchased from E-merck (Mumbai, India). Xanthine (XN), N-hydroxy succinamide (NHS), and 1-Ethyl-3-(3-dimethylaminopropyl) carbodiimidehydrochloride (EDC) have been procured from Himedia, India.

All solutions were prepared using purified water with the resistivity of 18.2 MΩ.cm from water purification system (Model no: arium®611UF, Sartorius stedim biotech GmbH, Germany). Nutrient broth (NB) culture media (peptone, 5 g L^{-1}; NaCl, 5 g L^{-1}; yeast extract, 2 g L^{-1}; beef extract 1 g L^{-1}; pH 7.0 ± 0.2) and salt media (K_2HPO_4 1; KH_2PO_4, 0.5; NaCl, 0.5; yeast extract, 0.5; $FeSO_4{\cdot}7H_2O$, 0.1; $MgSO_4{\cdot}7H_2O$, 0.1; in g L^{-1}) autoclaved at 121 °C for 15 min before use. Selective xanthine media (SXM) were prepared by adding sucrose (3.0 g L^{-1}) and xanthine (0.2 g L^{-1}) just before inoculation in a sterile condition of laminar airflow (ESCO, U.K). Details of the apparatus were described in electronic supplementary materials.

2.2. Culture

Xanthine oxidoreductase (XOR) producing bacterial strain *Pseudomanas aerogenosa* strain CEBP1 (NCBI id: JQ894531), isolated from alkaloid enrich soil in the laboratory, was screened for isolation of target XOR gene from genomic DNA. The bacterial strain was grown in SXM at 37 °C with 150 rpm overnight in a shake flask incubator to activate its XOR gene. Cell-free extracellular extract (CFE) was collected after separation of the biomass of the microbial culture for extraction of genomic DNA by centrifugation at 8000 rpm for 10 min at 10 °C.

2.3. Cloning, expression and purification of xanthine oxidoreductase (XOR)

Genomic DNA was isolated using the standard phenol–chloroform extraction method. The reverse and forward primer pair was designed as XOR-FP: 3′-GCT ATC CAT ATG ATG TCT AAC CAT CGC AAG CCG CAC AAG AGC CAG GAA GAG C-5′; XOR-RP: 5′-GCT CGA GGG CCG GTT CGA CCG CGG CGT C-3′; having restriction digestion site for NdeI and XhoI respectively to amplify the gene. The PCR was performed using Pfu DNA polymerase (BioBharati Cat # BB-E0020) followed by the PCR condition: heating at 94 °C/5 min, denaturation at 94 °C /1 min, annealing at 67 °C/1 min, elongation at 72 °C/5 min, final elongation at 72 °C/7 min for 30 cycles. *E. coli* strain DH5α was used for initial cloning and multiplication of recombinant plasmid. The cloning of the XOR gene was done in pET22b (Amp +) vector containing C-terminal His tag for easy purification.

The recombinant clone was transformed into E. coli strain BL21 DE3 Rosetta (Amp+ & Chl +) host. The transformed colony was first inoculated into LB medium (pH 7.2) with proper antibiotic selection and incubated at 20 °C for 16 h with 0.2 mM IPTG induction. Cell biomass was collected by centrifugation at 2881 rcf for 10 mins at 4 °C using a cold centrifuge (Table top refrigerated high-speed centrifuge, Model Z 32HK, Hermle, Germany) with a rotor diameter of 10.5 cm. The pellet was resuspended in lysis buffer (25 mM Tris-HCl (pH-7.5); 150 mM NaCl; 0.5% Triton-X-100; 5% Glycerol). The overexpressed protein was purified using Ni-NTA matrix (BioBharati, Cat No: BB-NA002) in equilibration buffer (25 mM Tris, 100 mM NaCl, pH 7.5) and analyzed by SDS-PAGE. The final protein was eluted using a varying concentration of imidazole. Purified protein was stored after dialysis in 50 mM potassium phosphate buffer (PPB), pH 7.5. The enzyme assay was performed as described in our previous publication [11]. Briefly, 0.5 mM XN, 0.5 mM MTT, 0.5 mM PMS, and 0.3 mM NAD + were mixed in PPB containing 1% triton X-100 at 20 °C, and enzymatic activity of the purified XOR was measured spectrophotometrically at 590 nm based on the reduction of MTT to formazan ($E_{590nm} = 8.8\ mM^{-1}cm^{-1}$)[11].

2.4. Biosynthesis of gold nanoparticles using extracellular supernatant

Gold nanoparticles (GNPs) were synthesized by adding auric chloride salt (1 mM) into the collected CFE and incubated for overnight to synthesize GNPs under continuous stirring through the green route at 40 °C without using any cytotoxic reducing chemicals and stabilizer. After incubation, the pale yellow color of the solution changed from ruby red to purple with the increase in incubation time. The biosynthesized gold nanoparticles (BSGNP) were collected after centrifugation at 13000 rpm for 15 min followed by washing thrice with deionized water. Dialysis was performed to remove all impurities of the culture media. A dried sample was stored for further study.

2.5. Preparation of BSGNP conjugated XOR enzyme

In the typical experiment, covalent immobilization of purified XOR with BSGNP was performed by EDC-NHS chemistry. The BSGNPs were dispersed in 5 mL of PPB (50 mM, pH 7.0) containing 20 mM EDC and 10 mM NHS for 2 h with continuous stirring for activation of –COOH

groups present on the surface of biomolecules capped gold nanoparticles. XOR solution (1 mg/mL) was then added to the activated BSGNP at 4 °C under continuous stirring for 1 h. The XOR-bound gold nanoparticles were formed by covalent bond formation between $–NH_2$ groups of XOR and activated $–COO^-$ group of BSGNP. The resulting solution was washed several times until no enzyme remained in the supernatant. After washing, the BSGNP conjugated XOR (Au-XOR) was resuspended in the PPB (50 mM, pH 7.0) and stored at −20 °C until use. The stability and enzymatic activity of Au-XOR were monitored for further use in the development of a biosensor.

The interaction between BSGNP with XOR was investigated by UV, Fluorescence (FL), and circular dichroism (CD) spectroscopy. Intrinsic Fluorescence quenching of tryptophan (Trp) studies was performed to predict the preferred interaction of BSGNP with XOR using FL spectrophotometer (Model: F-7000FL, Hitachi, Tokyo, Japan). Trp fluorescence intensity of native XOR was measured with increasing concentration of BSGNP to explore the main interaction. Circular dichroism (CD) spectra were recorded on Jasco 400 spectrophotometer (JASCO International Co., Ltd., Hachioji, Tokyo, Japan) at 10 °C in the range of 280 to 190 nm using a quartz cuvette of 1 cm optical path length was used. Molar ellipticity (θ, deg cm^2dmol^{-1}) was measured every 2 s with an integration time of 50 nm min^{-1}. CD spectra were recorded after averaging five scans for XOR and Au-XOR to ensure the structural integrity of the enzyme after interaction with different concentrations of nanoparticles. Alteration of the secondary structure of XOR (10 μg mL^{-1}) was calculated by comparing the molar ellipticity at 222 nm (θ_{222}).

2.6. Fabrication of enzyme electrode by immobilization of BSGNP-XOR on the modified polymeric matrix

Three electrode systems containing glassy carbon working electrode (GCE, WE), platinum counter electrode (PtE, CE), and Ag/AgCl (3 M NaCl) reference electrode (RE) were used for electrochemical analysis. The electrodes were connected with AUTOLAB PGSTAT 12 potentiostat/galvanostat (Ecochemie B.V. Netherlands) electrochemical analyzer. The electrodes (WE and CE) were polished with 0.05 μm alumina powder, followed by ultrasonication in ethanol and deionized water (1:1) for 5 min before modification. These were rinsed thoroughly with deionized water before the experiment.

Firstly, commercial MWCNT was functionalized before electrodeposition by strong acid (H_2SO_4: HNO_3 in 3:1) hydrolysis according to our earlier report [17] under sonication for 4 h. 0.03% (w/v) fMWCNT was sonicated for 30 min and added to 20 mM EDOT solution of acetonitrile/water in presence of 100 mM KNO_3 (act as a dopant) for further sonication of 30 min. The black stable suspension of fMWCNT dispersed PEDOT was used for one-step rapid co-electrodeposition of fMWCNT-PEDOT:NO_3 film at an applied potential span of −0.9 to + 1.8 V at a scan rate of 50 $mV.s^{-1}$ for nine cycles on the surface of glassy carbon working electrode (GCE). The modified fMWCNT-PEDOT:NO_3/GCE was immersed in 10 mM EDC solution for 30 min and 10 mM NHS was added to activate free carboxylic groups of the modified electrode followed by stirring for another 30 min. To remove nonspecific chemicals the modified electrode was washed thoroughly with buffer just before immobilization of GNP-conjugated XOR enzyme [Au-XOR]. Finally, the purified XOR (1U) was incubated with 0.01 mM BSGNP to enhance the storage stability and enzymatic activity. The enzyme molecules were covalently bound to the activated polymeric nanocomposite via the formation of an amide bond between the primary amine of XOR with stable NHS–carbodiimide–ester of a polymeric matrix without altering its activity. Since AuNP has a good affinity towards sulpher group, Au-S bond may also form between the enzyme and polymeric matrix. A schematic diagram of stepwise electrode fabrication of the proposed Au-XOR/fMWCNT-PEDOT/GCE sensor is shown in Scheme 1.

3. Results & discussion

3.1. Cloning, expression, and purification of XOR enzyme

About ten colonies of the appropriate clone for the XOR gene were selected and transformed into the *E.coli* host (BL21 DE3 Rosetta). Fig. 1a displays the schematic design of pET22b plasmid that was present in the appropriate clone. The plasmid contained T7 promoter region responsible for XOR enzyme synthesis coding DNA sequence followed by His tag for better purification with two restriction endonuclease (NdeI and Xho I) cutting sites. The Rosetta cell having successfully transformed recombinant plasmid (pET22b) was selected in Amp + Chl containing LB plate. Fig. 1b shows 1 % agarose gel image of PCR product of XOR gene having 2.4 kb of nucleotide bases. The successful cloning of the target gene into pET22b vector was confirmed by single (NdeI) and double digestion (NdeI and XhoI) of recombinant clone with restriction endonuclease (Fig. 1c). The nucleotides sequence of the target XOR gene was confirmed by DNA sequencing analysis. The XOR gene was expressed in *E. coli* BL21(DE3) host cell by IPTG induction and the over-expressed protein band was evident in SDS-PAGE. In Fig. 1d, the over-expressed protein band was observed at approximately 89 kDa in the IPTG induced cell against the uninduced one where no band of interest existed. The expressed XOR protein was purified by affinity chromatography using NiNTA matrix and different elution fraction was run in SDS-PAGE (Fig. 1e). After purification and dialysis process, the yield of XOR enzyme from one liter of *E. coli* BL21 host cell with pET22b was 15 mg of protein with specific enzyme activity of 136 $U.mg^{-1}$. The enzymatic activity of the purified XOR was enhanced 25.8 times compared to the crude extract [11].

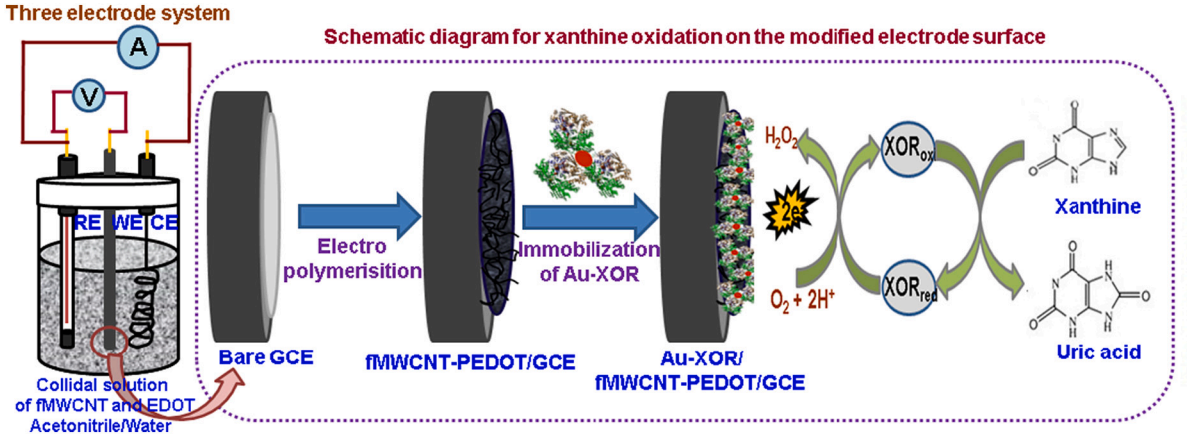

Scheme 1. Schematic diagram of stepwise electrode fabrication of Au-XOR/PEDOT/fMWCNT/GCE for detection of xanthine.

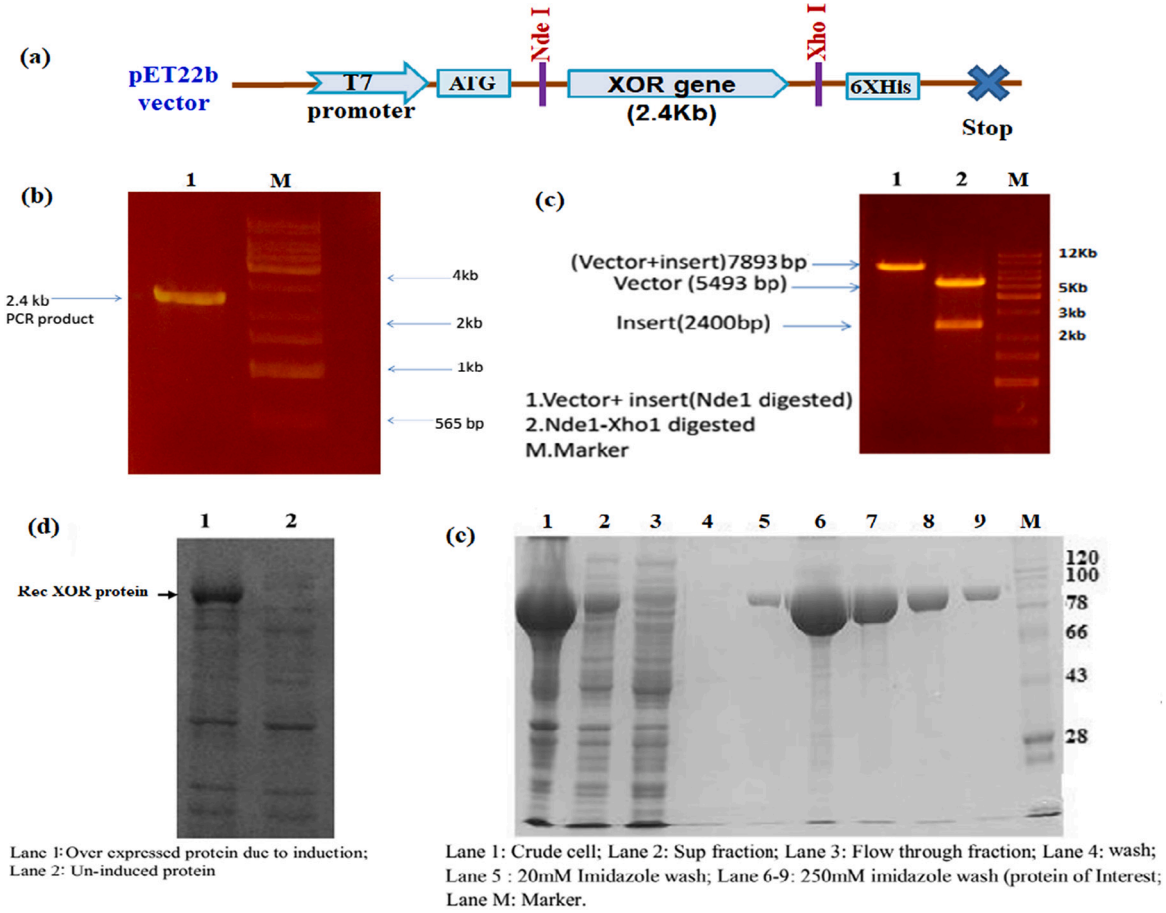

Fig 1. Amplification, expression and purification of XOR.(a) schematic diagram of pET22b plasmid with insert ORF of XOR enzyme, (b) Agarose gel electrophoresis of XOR gene (2.4 kb), (c) Checking of recombinant plasmid clone of XDH in pET22b (lane 1: linearized (NdeI digested) recombinant plasmid of XOR clone, lane 2: Double digested clone of the recombinant plasmid with NdeI and XhoI; lane M: High molecular weight DNA Marker), (d) Overexpression of recombinant XDH enzyme (lane 1: Overexpressed protein due to induction; lane 2: Un-induced protein), (e) SDS-PAGE of total protein of bacterial cell and purified recombinant XOR (lane 1: crude cell; lane 2: Sup fraction; lane 3: Flow-through fraction; lane 4: wash; lane 5: 20 mM Imidazole wash; lane 6–9: 250 mM imidazole wash (protein of Interest; lane M: Marker).

3.2. Characterization of BSGNP from Pseudomonas sp strain CEBP1

The biosynthesized gold nanoparticle (BSGNP) was initially characterized by various spectroscopic and microscopic techniques (Fig. 2). Fig. 2a depicts the surface resonance peak of BSGNPs at 520 nm in CFE of NB and a sharp peak at 560 nm was observed in SXM. This slight shifting of absorption peak might be due to the covalent or electrostatic interaction of functional groups of biomolecules with the surface of GNP. The inset of Fig. 2a displays the colloidal gold suspension in NB and SXM. Au^{3+} was reduced to Au^{0} by the reducing activity of various biomaterials (e.g. enzyme, protein, polysaccharide, metabolites) in the CFE. These could also act as capping agents to stabilize the BSGNPs [14,27]. Faster GNP formation in SXM might be due to the presence of uric acid (UA) (having antioxidant activity) as a metabolic product of xanthine. The zeta potential value of BSGNPs in SXM was −20.6 mV, which confirmed its higher stability than BSGNP synthesized in NB (Au-NB) ($\zeta = -14.2$ mV). Inset of Fig. 2b shows the accumulation of GNPs (red arrows) on the surface of the bacterial cell of CEBP1 when it was grown in $HAuCl_4$ containing media. It same was also confirmed by the EDX spectra (Fig. 2c) of the BSGNP. Fig. 2d depicts the crystalline nature of BSGNP as the diffraction peaks of XRD spectra at 2θ values of 31.97, 38.52, 45.76, 66.41, 75.61, and 84.53 were observed for the Bragg reflection of lattice plane (110), (111), (200), (220), (311), and (222), respectively [14,17]. Fig. 2e depicts the FTIR spectra of CFE and BSGNP to identify the biological moieties involved in the green synthesis of GNP. Two absorption bands appeared in the range of 3200–3400 cm^{-1} and these are due to the N-H stretching vibration of 1° and 2° amines, amides [27,28]. A peak at 1620 cm^{-1} for amide-I indicates the interaction of proteins onto the surface of BSGNPs [27]. An absorption band at 1301 cm^{-1} in CFE disappeared and a sharp peak at 1242 cm^{-1} appeared in GNP. This might be due to a change of C-N stretching vibrations. The peaks at 2936 cm^{-1} and 686 cm^{-1} indicate the stretching of the sulphydryl group depicting that gold nanoparticle was thiolated by –SH group of cysteine of protein molecules [28,29]. Peaks observed at 1447 cm^{-1}, 1045 cm^{-1}, and 960 cm^{-1} were due to vibrational frequencies of C-H bending, alkoxy C-O, and O-H bond of carboxylic acid, respectively, and might be responsible for the catalytic reduction of $AuCl_4^-$ to form elemental GNP [16]. The results suggested that the biomolecules including proteins, secondary metabolites, played major roles in the biosynthesis of GNP [14,16].

3.3. Interaction study of BSGNP with the purified xanthine oxidoreductase

Fig. S1 depicts the change of UV–vis absorption spectra of XOR in presence of BSGNP. It suggests weak complex formation between XOR and BSGNP that could facilitate more affinity towards xanthine for oxidation reaction [30,31]. The detailed calculations for UV, PL, and CD spectra are described in the supplementary document. Fig. S2 shows the Tryptophan fluorescence emission spectra (Ex 279 nm) of XOR with an

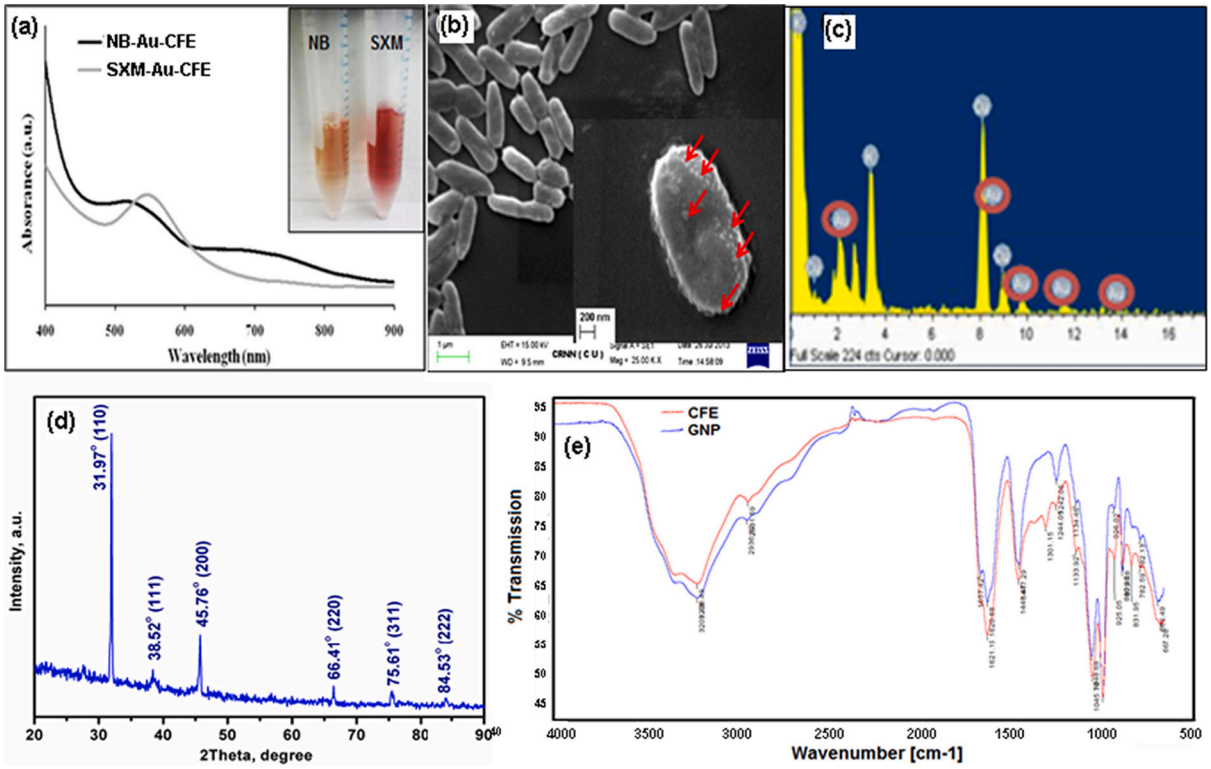

Fig. 2. (a) UV/vis spectra of gold nanoparticles synthesized by *P. aerogenosa strain CEBP1* grown in Nutrient broth (NB) and selective xanthine media (SXM); inset: the color change of the gold nanoparticles suspended solution of NB and SXM after 24 h incubation with 1 mM auric chloride in CFE, (b) SEM micrograph of CEBP1, inset: GNP precipitated (indicating by red arrows) on the surface of CEBP1 when it was grown in SXM, (c) EDX spectra of BSGNP, (d) XRD spectra of BSGNP isolated from CEBP1 in SXM, (e) FTIR spectra of only extracellular extract and GNP synthesized in the extract.

increasing concentration of BSGNP. The emission intensity of XOR at 340 nm decreased gradually with blue shift and quenching constants (K_{SV}) were calculated from the slope of Stern-Volmer (F_o/F versus [BSGNP]) plot as 1.419 M^{-1}. The static type fluorescence quenching indicated ground state complex formation between AuNPs and purified XOR [30,31]. The alteration of the secondary structure of XOR due to interaction with BSGNP (0 to 100 μM) was investigated by performing CD spectra (Fig. S3) at the far UV region (195–270 nm) [28,30,32]. The percentage of α-helicity decreased from 63% to 50% due to the incorporation of 10 μM BSGNP. The reduced α-helix content in Au-XOR might be due to alteration in the spatial arrangement of intra-molecular amino acid residues [27]. The activity of enzymes may vary due to the unfolding of the bound proteins to NPs in a way to expose hidden epitopes that play a role in either induction of enzymatic activity or reduce its activity [33,34].

Bright-field TEM micrograph (Fig. S4) shows a slight tendency of agglomeration of BSGNP due to variation of the ratio of enzyme concentration to form a more stable Au-XOR complex. Since the isoelectric focusing point (pI) of XOR is nearly about 4.2, it has a negative charge at pH 7.0 [8,9]. It may be suggested that the negatively charged XOR acted as a stabilizer to form a stable colloidal solution of XOR conjugated GNP (Au-XOR).

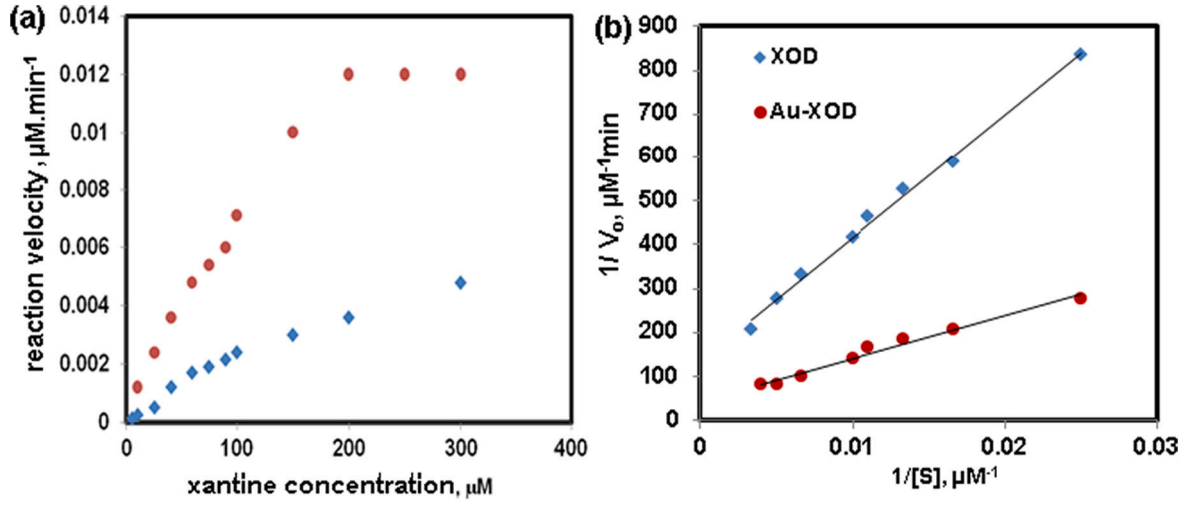

Fig. 3. Enzyme activity (a) and Michelis-Menten plot (b) for XOR (◆) and BSGNP conjugated XOR(●).

The highest enzyme activity was found with the interaction of BSGNP in the ratio of 1:10 (Au:XOR) compared to 1:5, 1:2, and 10:1. Fig. 3 depicts the enzymatic activity (a) and Michaelis-Menten plot(b) for the reduction of MTT by free XOR enzyme and Au-XOR (1:10) with increasing concentration of xanthine at pH 7.4 and 25 °C. The value of Michaelis-Menten constants (K_m) of free XOR and Au-XOR were found to be 15.1 and 12.2 μM, respectively. A smaller value of K_m indicates closer interaction of the BSGNP conjugated XOR enzyme with the substrate to form a stable enzyme-substrate (ES) complex [28,34,35]. The value of V_m also got enhanced from 39.6 to 44.5 μM.min^{-1} after incubation with BSGNP. The result suggests that the enzymes capped on the BSGNP could retain their ability to perform nucleophilic attacks to XN like free XOR and there was no influence on the product release in the rate-limiting step [34,35]. The enzyme-GNP complex retained its activity 91 % at 4 °C for 25 days and after six months of storage at −20 °C enzyme activity remains 89 % of its initial.

3.4. Characterization of modified electrode Au-XOR/fMWCNT-PEDOT/GCE

In Fig. 4a, the normalized Raman peaks (curve i and ii) nearly at 1346 cm^{-1}, 1585 cm^{-1}, 2700 cm^{-1} represent the D band, G band, and 2D band of MWCNT, respectively. The increase of intensity ratio of D and G band (I_D/I_G) from 1.054 to 1.168 indicates enhancement of defects in MWCNT after functionalization with acid treatment [36]. Fig. 4a, curve iii depicts the major Raman peaks at 1502 and 1562 cm^{-1} attributed to the $C_\alpha = C_\beta$ asymmetric stretching vibration of thiophene rings in the middle and at the end of the PEDOT chains. The Raman spectra of fMWCNT-PEDOT (Fig. 4b, curve iv) are nearly similar to only PEDOT (Fig. 4b, curve iii) except that a peak arises at 2870 cm^{-1} indicating the presence of fMWCNT in the composite. The Raman peak shift from 1562 to 1568 cm^{-1} was associated with electronic charge transfer between the fMWCNT with the conjugated thiophene ring of PEDOT, and suggests the formation of polymeric nanocomposite [5,36,37]. FTIR spectra of PEDOT (Fig. 4b, curve i) depicts multiple peaks corresponding to asymmetric stretching of C = C (1520 cm^{-1}), inter-ring stretching vibration of C-C (1337 cm^{-1}), C-O-C bending (1205 cm^{-1}, 1089 cm^{-1}) in ethylenedioxy group, and C-S-C bond (981, 916, 841, and 692 cm^{-1}) in thiophene ring [38]. The increased peak intensity around 2923 to 2831 cm^{-1} appears for assymmetric and symmetric stretching of C-H bond of phenyl ring due to the attachment of PEDOT with fMWCNT (Fig. 4b, curve iii) in comparison to fMWCNT (curve ii). Characteristic FTIR peaks of fMWCNT-PEDOT at 1637 and 1386 cm^{-1} could be attributed to –COO$^-$ asymmetric bending and phenyl ring stretching, respectively [5]. A broad band showed around 3436 cm^{-1} corresponds to –OH stretching vibration in both fMWCNT and fMWCNT-PEDOT. After immobilization of Au-XOR on fMWCNT-PEDOT/GCE (Fig. 4b, curve iv) peaks appear in the range of 3600–3400 cm^{-1} and 1611 cm^{-1} corresponding to N-H stretching, N-H bend due to the formation of an amide bond between the free carboxyl group of fMWCNT to the amino group of enzyme molecules, which is consistent with the XRD results. In Fig. 4c, the pristine fMWCNT depicts a broad diffraction peak ranging

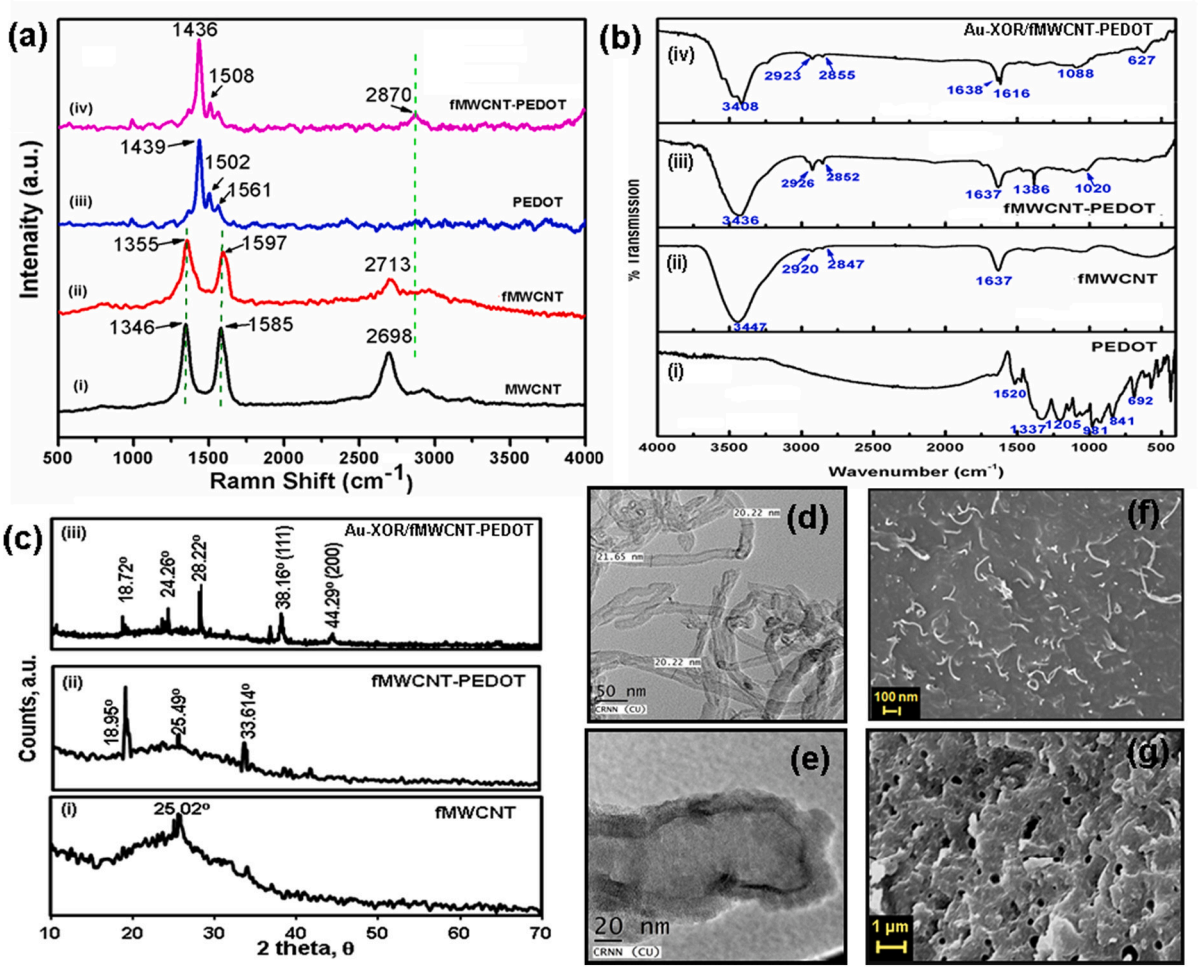

Fig. 4. (a) Raman spectra of MWCNT(i), fMWCNT(ii), PEDOT(iii), fMWCNT-PEDOT(iv); (b) FTIR spectra of fMWCNT(i), PEDOT(ii), fMWCNT-PEDOT(iii), Au-XOR/fMWCNT-PEDOT(iv); (c) XRD spectra of fMWCNT(i), fMWCNT-PEDOT(ii), Au-XOR/fMWCNT-PEDOT(iii); (d,e) TEM micrograph of fMWCNT and fMWCNT-PEDOT, respectively; (f, g) FESEM image of fMWCNT-PEDOT/GCE and Au-XOR/fMWCNT-PEDOT/GCE.

from 15° to 37° and centered at 25.49° (002). Fig. 4c, curve ii shows two peaks at 18.95° and 33.61° for fMWCNT/PEDOT:NO_3, indicating semi-crystalline nature of the polymeric nanocomposite. Au-XOR/fMWCNT-PEDOT (Fig. 4c, curve iii) demonstrates additional peaks at 2θ values of 38.16° (111), 44.29° (200), due to immobilization of fcc structured AuNP conjugated enzyme molecule, suggesting crystalline nature of the nanocomposite [5].

Fig. 4 d,e depicts the TEM micrographs of fMWCNT and PEDOT coated fMWCNT, respectively. The average diameter of as prepared fMWCNT was increased after electrodeposition of PEDOT on fMWCNT/GCE. It could be suggested that negatively charged fMWCNT (COO^-) was wrapped by PEDOT during polymerization through electrostatic interaction [39]. Fig. 4f,g depicts the FESEM image of electrodeposited PEDOT on fMWCNT/GCE and after immobilization of Au-XOR on fMWCNT-PEDOT/GCE, respectively.

3.5. Electrochemical behaviour of modified electrode

Fig. 5a shows cyclic voltammogram patterns during electrodeposition of fMWCNT doped PEDOT on the surface of bare GCE. It depicts a higher capacitive current compared to electrodeposition of only PEDOT on GCE (Fig. S5). The highest anodic peak current at 1.236 V for initiation of monomer (EDOT) oxidation gradually decreased due to the formation of diradical or bipolaron in the subsequent scans. Another oxidation peak at 0.375 V appeared for oxidation of the radical cations from the second cycle and the oxidation peak current increased with a positive potential shift towards 0.703 V after the tenth scan whereas the reduction peak shifted towards a negative potential (-0.121 to −0.169 V), indicating elongation of the polymeric chain of fMWCNT-PEDOT [5,40]. Fig. 5b depicts the Nquist plot of electrochemical impedance spectroscopy to investigate the change of conductivity of the modified electrode surface. Charge transfer resistance (R_{ct}) of bare/GCE, fMWCNT/GCE, fMWCNT-PEDOT/GCE were 150.59, 429.2, 59.15 Kohm, respectively. fMWCNT/GCE shows higher electron transfer resistance due to the presence of negatively charged functional groups such as hydroxyl, carboxyl on the surface of fMWCNT [17]. The R_{ct} value was reduced effectively after electropolymerization of conducting polymer PEDOT on fMWCNT/GCE; indicating faster electron transfer through the diffusion layer during oxidation of xanthine on the modified surface. Fig. 5c depicts the oxidation and reduction peak current of $Fe^{3+/4+}$ redox couple using modified electrodes. The highest peak current was observed at 0.308 V (curve ii) due to the porous conducting polymeric nanostructure of PEDOT/fMWCNT/GCE. But the peak height got reduced after immobilization of XOR (curve iii) due to inhibition of fast electron transfer caused by poor conductivity of biomolecules (eg. any enzyme like XOR). Thus it can partially block the layer to hinder electron transfer according to the previous report [17,22,41]. The peak current increased significantly for Au-XOR/fMWCNT-PEDOT/GCE (curve iv) owing to the interaction of AuNP with enzyme molecules. Nanoparticles create a favorable microenvirnment for fast electron transfer from the site of biomolecules to the electrode surface by increasing enzymatic activity [17,19,20,35].

The electroactive surface area (A_c) of the fMWCNT-PEDOT/GCE was calculated from the following Randles–Sevcik equation for the reversible process [32] by performing CV in 1 mM $Fe^{3+/4+}$ solution containing 0.1 M KCl (Fig S6) at different scan rates ($\nu = 0.01$ to 0.25 Vs^{-1}).

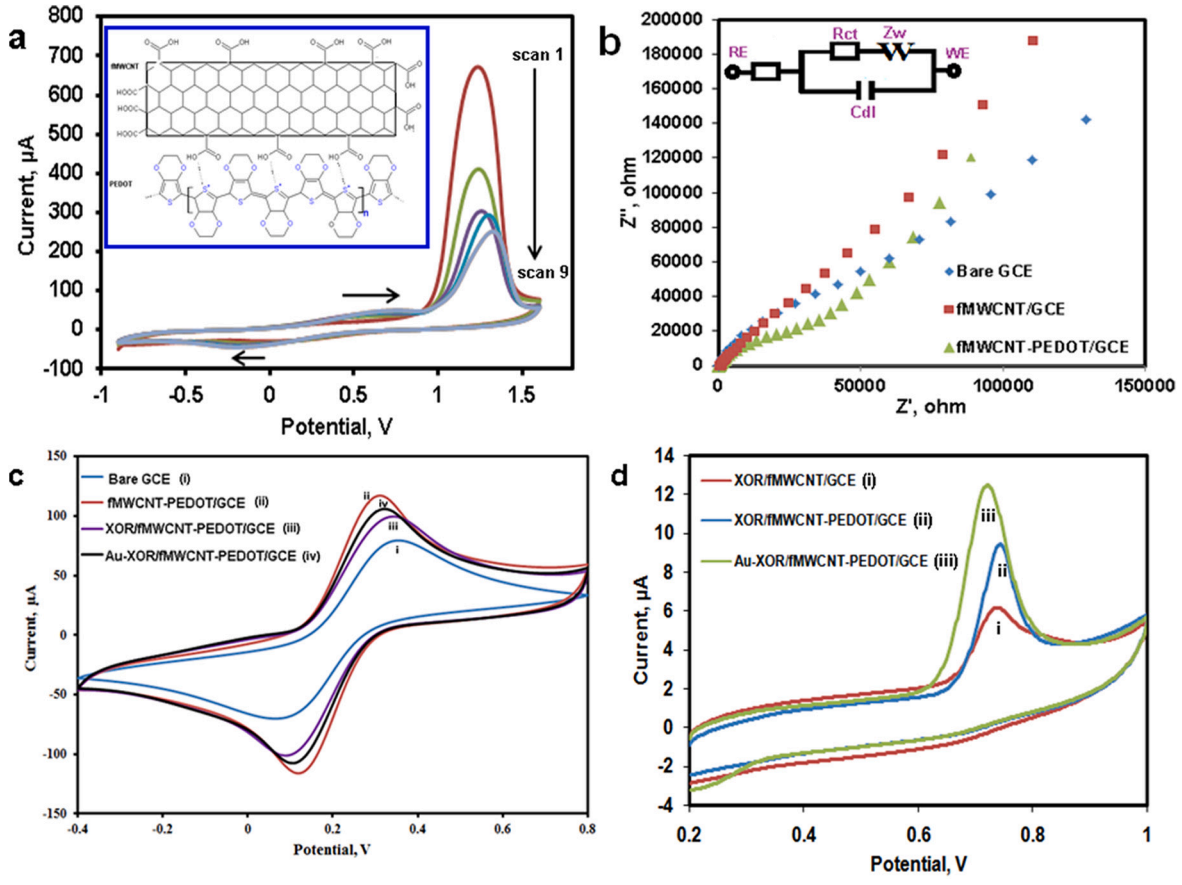

Fig. 5. (a) CV growth profile of fMWCNT doped PEDOT on GCE; (b) Nyquist plot of bare GCE, fMWCNT/GCE, fMWCNT-PEDOT/GCE; (c) CV of bare GCE (i), fMWCNT-PEDOT/GCE (ii), XOR/fMWCNT-PEDOT/GCE (iii), Au-XOR/fMWCNT-PEDOT/GCE (iv) in 0.1 M KCl solution containing 1 mM $[Fe(CN)_6]^{3-/4-}$; (d) CV of modified electrodes such as XOR/fMWCNT/GCE (i), XOR/fMWCNT-PEDOT/GCE (ii), Au-XOR/fMWCNT-PEDOT/GCE (iii) in 50 µM of xanthine containing PPB buffer;

$$I_p = \left(2.69X10^5\right)n^{3/2}A_c D_r^{\frac{1}{2}}v^{\frac{1}{2}}C \quad (2)$$

where, C, Dr, and n denote the concentration of the redox probe (mol.cm^3), diffusion coefficient (cm^{2}s^1), and the number of electrons transferred, respectively. The A_c of the modified electrode was found to be 0.6395 cm^2 i.e. ten times higher than the bare electrode (0.0707 cm^2) [5].

It was also proved by performing CV (Fig. 5d) at the potential span of 0.2 to 1 V in 50 μM xanthine containing 50 mM PPB (pH 7). The first cycle of CV measurements always showed maximum peak current for xanthine oxidation (Fig. S7) on the modified electrode surface and the peak current decreased gradually with consecutive scans due to nonavailability of enough substrate as well as deposition of product on the electrode surface during the subsequent scans. A significant increase in oxidation peak of xanthine at 0.721 V was observed for Au-XOR/fMWCNT-PEDOT/GCE (Fig. 5d, curve iii) compared to XOR/fMWCNT-PEDOT/GCE (Fig. 5d, curve ii) (E_{pa} = 0.742 V) and XOR/PEDOT/GCE (Fig. 5d, curve i) (E_{pa} = 0.736 V). The increase in the oxidation peak current could imply that AuNP conjugated XOR immobilized on fMWCNT-PEDOT/GCE displayed good catalytic activity and better stability toward oxidation of xanthine [17,22].

3.6. Effect of pH, and temperature of the modified electrode

The analytical performance of the proposed biosensor largely depends on the enzymatic activity of the immobilized enzyme at optimum pH and temperature. Fig. 6a depicts the CV of 75 μM xanthine in PPB at different pH and it was observed that the highest anodic peak current was obtained at pH 7 (Fig. S8). At pH > 7.0 and < 7.0, the oxidation peak height decreased due to reduced enzymatic activity of XOR at that pH [2,17,19,22,25]. The xanthine oxidation potential shifts towards less positive potential with increasing pH of the buffer (Fig. 6a). Inset of Fig. 6A shows the slope of Ep (V) versus pH is −0.052, closer to the theoretical value of Nernst equation i.e. 0.059 V pH^{-1}; indicating the involvement of equal number of electrons and protons during oxidation of xanthine on the modified electrode surface [17,22,25].

The effect of temperature on xanthine oxidation was monitored by varying the temperature of the electrolytic buffer from 4 to 60 °C (Fig S9). The oxidation peak current increased with temperature up to 40 °C and reduced at higher temperature as enzyme-catalytical reaction went faster with temperature until protein structure started to unfold [5,17,42–44].

3.7. Effect of potential scan rate on the oxidation of XN at Au-XOR/fMWCNT-PEDOT /GCE

Fig. 6b represents a linear relationship of scan rate variation and anodic peak current with the shift of oxidation peak towards a positive potential direction, suggesting surface-confined irreversible voltammetric reaction [5]. The increase of anodic peak current with the square root of the scan rate depicts the linear regression equation of $I_{pa}(\mu A) = 1.089\nu^{1/2} - 1.93$ with a correlation coefficient of $R^2 = 0.987$. The slope of log I_p versus log ν is 0.713, indicating diffusion control process of xanthine oxidation (plot shows in supplementary data, Fig S10A). Fig. S10B shows linear plot of E_p versus log ν with regression equation of $E_{pa} = 0.073\log\nu + 0.7974$ ($R^2 = 0.988$).

For an irreversible electrochemical process, Laviron's theory states the following equation to calculate the E_p of each reaction [32,45].

$$E_p = E^{o'} + \left(\frac{2.303RT}{\propto nF}\right)log\left(\frac{RT\,k^o}{\propto nF}\right) + \left(\frac{2.303RT}{\propto nF}\right)log\,\upsilon \quad (3)$$

where k^o is the standard heterogeneous rate constant, $E^{o'}$ is the formal standard redox potential, υ is the scan rate, ∝ is the transfer coefficient, and n is the electron transfer number. R, T, F are universal standards (R = 8.314 J.K^{-1}, T = 298 K, F = 96480C.mol^{-1}). The value $E^{o'}$ could be calculated from the intercept of E_p vs. υ linear curve, (E_{pa} = 0.4469 ν + 0.6694, R^2 = 0.988). The k^o value for XN oxidation on the modified electrode was calculated to be 1.766X10^3 s^{-1} i.e. higher than the electron transfer rate at bare electrode. The $\propto n$ value was calculated as 0.82. The α value was obtained from the Bard and Faulkner (2004) equation of

$$\alpha = \frac{47.7}{E_p - E_{p/2}}mV \quad (4)$$

where $E_{p/2}$ is the potential corresponding to half of the peak current (I_p). Therefore, α was obtained as 0.808, and n was calculated to be around 2, which shows a good similarity with previous reports [43,46–50].

It is well-known that the oxidation of XN in presence of XOR is a four-step reaction process involving one mole of water molecule for the turnover of the XOR [17,51]. Scheme 2 represents a detailed reaction mechanism of oxidation of XN to UA. After substrate binds to the active site of XOR, proton of Mo(VI)–OH is moved to the –COO$^-$ group of Glu 1261 residue that is present in the highly conserved active site of XOR. Activated Mo(VI)-O$^-$ makes a nucleophilic attack on XN to form Mo(IV). UA is formed via its protonation by Arg880 through the generation of

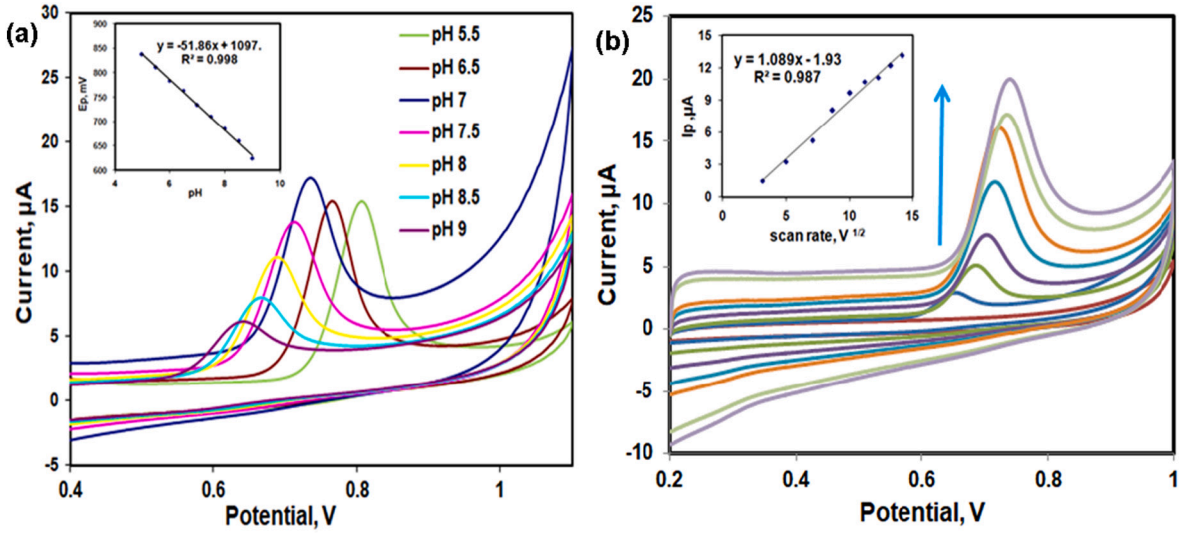

Fig. 6. (a) CV of 75 μM xanthine containing PPB at different pH, inset: plot of oxidation potential (E_p) versus pH; (b) change of CV with different scan rate (10, 25, 50, 75, 100, 150, 200 V), inset: plot of response current (I_p) versus scan rate.

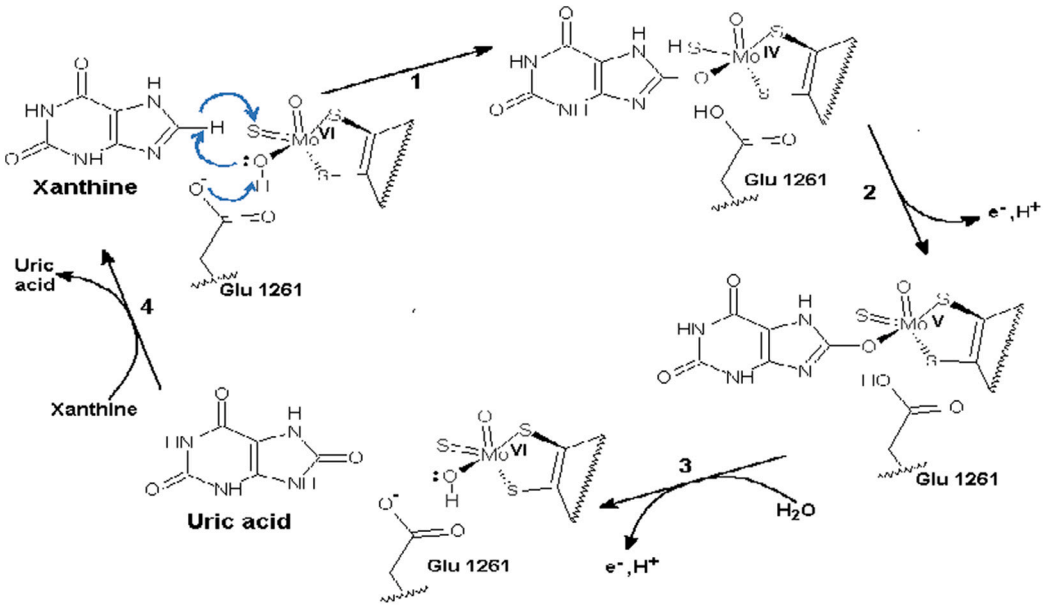

Scheme 2. Reaction mechanism of xanthine oxidation on XOR immobilized modified electrode surface.

two molecules of electron and hydrogen ion [51]. The electron transfers from the Mo(VI)-pterin unit to the acceptor through unequal iron-sulfur redox centers (Fe2/S2I and Fe2/S2II) and flavin adenine dinucleotide (FAD), respectively [9,52]. Finally, FAD is reduced to $FADH_2$, and Mo (IV)-SH is oxidized to its initial state of Mo(VI) = S by the addition of water.

$$\text{Xanthine} + \text{XOR (ox)} + H_2O \rightarrow \text{uric acid} + \text{XOR (red)} + 2e^- + 2H^+ \quad (5)$$

$$2e^- \rightarrow \text{working electrode} \quad (6)$$

3.8. Analytical performance of the biosensor

Differential pulse voltammetry (DPV) was conducted to achieve higher sensitivity and lower detection limit for quantification of xanthine at lower oxidation potential in PPB. The oxidation potential shifted towards negative potential remarkably with increasing modulation amplitude from 0.1 to 0.5 V with increase in peak current [5]. The optimized parameters for monitoring of XN oxidation were as follows: voltage range = -0.2 to 1.1 V, step potential = 6 mV, modulation amplitude = 0.3 V, modulation time = 0.05 s, interval time = 0.2 s. Fig. 7a depicts anodic peaks for XN oxidation at 0.434 V for 1 nM and peak potential shifts to positive direction with increase of XN concentration such as 20 μM of XN oxidized at 0.446 V and the peak shifts to 0.476 V for 150 μM of XN. The linear calibration curve for the range of 0.1 to 10 μM was $I_p(\mu A) = 1.1365[XN] + 0.0716$ ($R^2 = 0.996$); $I_p(\mu A) = 0.413[XN] + 2.2412$ ($R^2 = 0.994$) for 10–50 μM, $I_p(\mu A) = 0.1883[XN] + 12.907$ ($R^2 = 0.983$) for 50–200 μM of XN. The detection limit (LOD = $3*SD_{blank}$/slope) and quantification limit (LOQ = $10*SD_{blank}$/slope) was found to be 54.95 nM, 183.17 nM, respectively from the calibration curve of the lower range XN quantification. The proposed modified electrode showed better sensitivity i.e. 16.075 mA mM^{-1} cm^{-2} compare to previous reports [5,17].

The enzyme kinetics of the modified electrode was estimated from Michaelis–Menten plot of the reciprocal of the steady-state current (I_s) versus the reciprocal of the substrate concentration, ([S]) (Fig. 7b). For electrochemical analysis, the Michaelis-Menten equation can be represented as follows [17]:

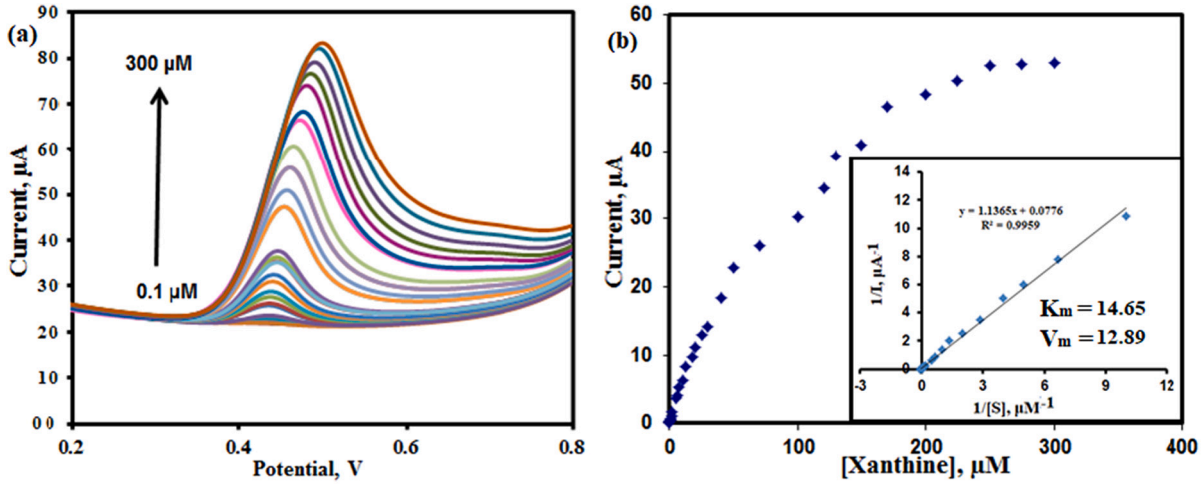

Fig. 7. (a) DPV response for the increasing concentration of XN (0.1 to 300 μM), (b) calibration plot for xanthine oxidation at Au-XOR/fMWCNT-PEDOT/GCE (inset: Michaelis–Menten plot for enzyme kinetics on the modified electrode surface).

$1/I_s = 1/I_{max} + [(K_m^{app} / I_{max}) 1/S]$ (7)

where,; I_{max} is the maximum current response (μA) at steady-state condition, and K_m^{app} is the [substrate] (μM) at which reaction velocity i.e. response current is half of I_{max}. The value of the apparent Michaelis–Menten constant [K_m^{app}] denotes the affinity of the enzyme to the substrate. The K_m^{app} value for Au-XOR/fMWCNT-PEDOT/GCE was found to be 14.65 ± 1.9 μM being a little higher than free Au-XOR (12.3 μM) might be due to loss of some catalytic site during immobilization of the enzyme on the electrode surface [28,32,34]. Thus the reaction velocity of the immobilized enzyme is slightly less than free Au-XOR. The Au conjugated XOR showed higher affinity to the substrate compared to the only XOR immobilized on the electrode surface due to better accessibility of the substrate to the active sites of the immobilized enzyme on the modified electrode surface.

3.9. Selectivity, Interference, reproducibility, and repeatability of the proposed biosensor

The selectivity of the proposed sensor was studied in the presence of various possible interfering agents such as dextrose (5 mM), sucrose (5 mM), ascorbic acid (AA, 0.1 mM), inosine (1.5 μM), citric acid, oxalic acid, L-glutamic acid (1 mM), inosine monophosphate (IMP, 1.5 μM), theobromine, and sodium ion (Na^+, 145 mM) (Fig. 8). In Fig. 8a, DPV responses of the interfering compounds in the potential scan of 0.2 to 0.8 V do not show any significant peaks corresponds to the oxidation peak of xanthine. Fig. 8b also depicts no significant influence on the amperometric signals for the addition of AA, UA, HX, and Na^+ with a deviation within ± 5%.

The reproducibility of Au-XOR/fMWCNT-PEDOT/GCE was elucidated by repetitive DPV measurements of XN (50 μM) 8 times using five individually modified electrodes. The reusability of the proposed biosensor was also examined by measuring 15 successive current responses of xanthine with the same modified electrode. No significant reduction of DPV response was found and the relative standard deviation (RSD) was obtained within 3.2 %.

The long-term stability of the proposed sensor was assessed by regular experiments for four months at seven days intervals while the electrode was stored at 4 °C. The electrode showed 99% stability for the first 21 days and the activity of the electrode for XN oxidation retained almost 92% of its initial response even after 4 months (Fig. S11).

The proposed sensor exhibited higher stability and sensitivity compared to the previous reports (Table 1) and this might be due to immobilization of Au-XOR through strong covalent bonding with the modified electrode surface [4,17,19,20,22,23,25,53]. Conjugation of AuNP with purified XOR also enhanced the storage stability and activity of the biosensor. It may be observed that sensor referred in reference 17 exhibited better detection limit and linear range. One, may however note that this work (17) used costly commercial xanthine oxidase whereas the present work used low cost in house xanthine oxidoreductase purified from an isolated bacteria. The present BSGNP conjugated XOR (Au-XOR) on the polymeric matrix of fMWCNT-PEDOT provided a favourable microenvironment for fast electron transfer during oxidation of xanthine, and gave faster response time (4 s), greater sensitivity (16.075 μA.μM-1.cm-2), and higher stability (4 months) compared to the above cited work. Also at optimized parameters of DPV analysis, the interference-free detection of xanthine was performed at lower oxidation potential i.e. 0.446 V, that helps to minimize the effect of interference during real sample analysis.

3.10. Real sample analysis

The possibility of the practical applicability of the proposed sensing matrix was judged by conducting experiments with human serum and urine samples collected from the pathological laboratory. The fish and meat samples were purchased from the local market. Real samples were used following the institutional guidelines and relevant laws. The samples were prepared according to our previous report [17]. The accuracy of the sensor was examined by the addition of standard XN solution to the twenty times diluted real samples in the electrolytic buffer [17]. The DPV responses were monitored to quantify the amount of XN in the real sample from the calibration plot and corrected by the dilution factor. The analytical performance of the proposed sensor was compared with standard HPLC data. Table 2 shows the variation of recovery range from 96.86 to 105.13 % for the detection of xanthine with a relative error of 0.45 to 3.13 %. The sensor depicts excellent reliability in comparison with HPLC results with good correlation (y = 1.0171x + 0.0265, r = 0.999, significant at 1% level), suggesting excellent applicability of the biosensor for the quantification of xanthine in real samples.

4. Conclusions

In conclusion, it can be stated that BSGNP conjugated recombinant XOR enhanced enzymatic activity and storage stability compared to free XOR. BSGNP facilitated rapid electron transfer through the polymeric matrix of the modified electrode. The modified electrode of Au-XOR/fMWCNT-PEDOT/GCE exhibited low detection limits (54.95 nM), high sensitivity (16.075 $\mu A.\mu M^{-1}.cm^{-2}$), and rapid response (4 s) at low oxidation potential (0.446 V) for the detection of xanthine in real samples. It also showed long-term storage stability as the enzyme molecules bound covalently with the biocompatible polymeric nanocomposite modified electrode. The sensor exhibited 85% operational stability even after 83 experiments and retain around 92% storage

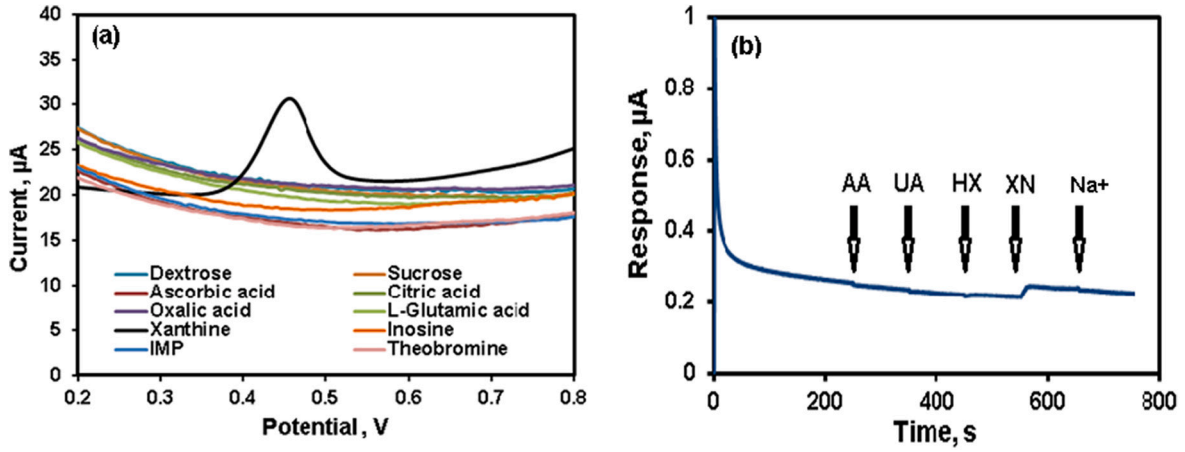

Fig. 8. (a) DPV responses of interfering substances in the potential range of 0.2–0.8 V in 50 mM. PPB (pH 7). (b) Amperometric response of interfering substances such as ascorbic acid (AA), uric acid (UA), hypoxanthine (HX), sodium ion (Na^+) using WE: Au-XOR/fMWCNT-PEDOT/GCE, RE: Ag/AgCl, CE: platinum wire.

Table 1
Analytical characteristics of some recently developed biosensors for detection of xanthine.

Reference	Electrode modification	Method of immobilization	Eapp / technique (V)	Optimum pH	Linear range (μM)	Detection limit (μM)	Sensitivity	Response time(s)	Storage stability	Analyte/ Applications
Devi et al, 2012[22]	XO/Au-ppy/ /PtE	covalently	0.4 V vs Ag/AgCl / amp	7.2	0.4–100	0.4	–	4	100 days (40% loss after 200 use)	XN/ fish, chicken, pork, and beef meat
Villalonga et al, 2012 [20]	Naf/XO-CD/ pAuNP/SWNT/ GCE	Physico-adsorption	0.65 V vs Ag/AgCl / amp	7.0	0.05–9.5	0.04	0.152 μA μM^{-1}	–	–	–
Dervisevic et al. 2015 [25]	Poly(GMA-co-VFc)/REGO-Fe_3O_4/XO	Physico-adsorption	0.35 V vs Ag/AgCl / Amp	7.0	2–36	0.17	0.17 μAM^{-1}	3 s	25 days (<80 % retain)	XN/ Fish,
Çevik et al. 2015 [19]	XO/AuNP/ PtNP/MWCNT/ GCPE	Physico-adsorption	0.8 V vs Ag/AgCl / Amp	7.0	2–50	–	–	–	48 h	XN
Sen and sarkar 2015[17]	XO/fMWCNT/ Au-PPD/GCE	Covalent	0.625 V vs Ag/AgCl / DPV	7.0	0.01–300	$1.2X10^{-2}$	14.03 μA μM^{-1} cm^{-2}	-6	4 months (91% retain after 210 uses)	XN/ fish, blood, urine
Dervisevic 2017[2]	XO@Chitosan-polypyrrole-gold NPs	Covalent	0.7 V vs Ag/AgCl/ Amp	7.0	1–200	0.25	1.4nA.μM^{-1}.	8	18 days (retained 85% of its initial activity	XN/ fish, chicken, beef
Wang 2019[3]	XOR@Cu-MOF/ SA	Physico-adsorption	0.65 V vs Ag/AgCl / DPV	7.5	0.01–10	$6.4X10^{-4}$	–	–	3 weeks (up to 100 times	XN, HX/ Chilled Seafish
Yazdanparast et al., 2019 [4]	XO/Poly(L-Asp)/MWCNT/ GCE	covalently	0.68 V vs Ag/AgCl / DPV	7.4	0.001–50.0	3.5×10^{-4}	–	35 s	2 weeks (90 % retain)	XN/ Fish, meat
Khan 2020 [54]	GCE/PEDOT: PSS-AuNPs	–	0.76 V vs Ag/AgCl / DPV	7.0	0.005–1	$3X10^{-2}$	–	–	4 weeks (<10% loss)	XN/ fresh fish, meat
This work	Au-XOR/ fMWCNT-PEDOT/GCE	covalent	0.446 V vsAg/AgCl / DPV	7	0.1–10	5.45X 10^{-2}	16.075 μA.μ M^{-1}.cm^{-2}	4	4 months (92% of its initial response)	XN/ fish, meat, blood, urine

reduced expanded graphene oxide (REGO); iron oxide (Fe_3O_4) nanoparticles; poly(glycidyl methacrylate-co-vinylferrocene) (P(GMA-*co*-VFc)), glassy carbon paste electrode (GCPE).

Table 2
Determination of xanthine in real samples using proposed Au-XOR/fMWCNT-PEDOT/GCE sensor.

Sample Name	Added (μM)	Found (μM) by Biosensor	Original (μM) by HPLC	Relative Error (%)	Recoveries (%)	RSD (%)
Fish 1	0	5.1	5.21	2.111	97.89	1.498
	10	14.75	14.98	1.535	98.46	0.518
	20	24.82	25.021	0.803	99.19	0.369
Fish 2	0	3.09	3.19	3.135	96.87	1.487
	10	13.45	13.71	1.896	98.10	0.620
	20	24.01	24.75	2.989	97.01	0.899
Meat 1	0	5.42	5.58	2.867	97.13	1.784
	5	10.82	10.96	1.277	98.72	1.202
	10	15.57	15.64	0.448	99.55	0.418
Serum 1	0	1.31	1.291	1.472	101.47	0.764
	5	6.23	6.351	1.905	98.09	0.579
	10	11.43	11.273	1.393	101.39	0.808
Urine 1	0	0.41	0.39	5.128	105.13	3.278
	5	5.39	5.45	1.101	98.90	0.586
	15	15.46	15.76	1.904	98.10	0.625

* All the experimental data showing P-value (n = 5) < 0.05.

stability after 4 months. The proposed biosensor also depicted good reproducibility (RSD = 3.2%) and repeatability for real sample analysis. Thus, it could be used for real sample analysis since it gave excellent correlation (R^2 = 0.999) with HPLC results. This unique, non-toxic, methodology could be used to fabricate other biosensors for rapid analysis of various analytes of our daily life.

CRediT authorship contribution statement

Sarani Sen: Conceptualization, Methodology, Data curation, Formal analysis, Investigation, Software, Writing – original draft. **Priyabrata Sarkar:** Supervision, Resources, Validation, Writing – review & editing.

Declaration of Competing Interest

The authors declare that they have no known competing financial interests or personal relationships that could have appeared to influence the work reported in this paper.

Acknowledgments

This study was funded by Department of Biotechnology, Government of India [No. BT/PR13282/NNT/28/802/2015]. The authors are thankful to Centre for research in Nanoscience and Nanotechnology (CRNN, CU) for SEM, FESEM. TEM facilities.

Appendix A. Supplementary material

Supplementary data to this article can be found online at https://doi.org/10.1016/j.ijbiomac.2021.12.094.

References

[1] V. Scognamiglio, F. Arduini, G. Palleschi, G. Rea, Biosensing technology for sustainable food safety TrAC, Trends Anal. Chem. 62 (2014) 1–10.

[2] M. Dervisevic, E. Dervisevic, E. Çevik, M. Şenel, Novel electrochemical xanthine biosensor based on chitosan–polypyrrole–gold nanoparticles hybrid bio-nanocomposite platform, J. Food Drug Anal. 25 (3) (2017) 510–519.
[3] Z. Wang, B. Ma, C. Shen, O.-M. Lai, C.-P. Tan, L.-Z. Cheong, Electrochemical Biosensing of Chilled Seafood Freshness by Xanthine Oxidase Immobilized on Copper-Based Metal-Organic Framework Nanofiber Film, Food Anal. Methods 12 (8) (2019) 1715–1724.
[4] S. Yazdanparast, A. Benvidi, S. Abbasi, M. Rezaeinasab, Enzyme-based ultrasensitive electrochemical biosensor using poly(l-aspartic acid)/MWCNT bio-nanocomposite for xanthine detection: A meat freshness marker, Microchem. J. 149 (2019) 104000, https://doi.org/10.1016/j.microc.2019.104000.
[5] S. Sen, P. Sarkar, A simple electrochemical approach to fabricate functionalized MWCNT-nanogold decorated PEDOT nanohybrid for simultaneous quantification of uric acid, xanthine and hypoxanthine, Anal. Chim. Acta 1114 (2020) 15–28.
[6] A.A. Ejaz, W. Mu, D.H. Kang, C. Roncal, Y.Y. Sautin, G. Henderson, I. Tabah-Fisch, B. Keller, T.M. Beaver, T. Nakagawa, R.J. Johnson, Could uric acid have a role in acute renal failure? Clin. J. Am. Soc. Nephrol. CJASN 2 (1) (2007) 16–21.
[7] M. Dervisevic, E. Dervisevic, M. Şenel, Recent progress in nanomaterial-based electrochemical and optical sensors for hypoxanthine and xanthine. A review, Mikrochim Acta 186 (12) (2019) 749.
[8] M. Bortolotti, L. Polito, M.G. Battelli, A. Bolognesi, Xanthine oxidoreductase: One enzyme for multiple physiological tasks, Redox Biol. 41 (2021) 101882, https://doi.org/10.1016/j.redox.2021.101882.
[9] T. Nishino, K. Okamoto, The role of the [2Fe-2s] cluster centers in xanthine oxidoreductase, J. Inorg. Biochem. 82 (1-4) (2000) 43–49.
[10] R. Hille, J. Hall, P. Basu, The mononuclear molybdenum enzymes, Chem. Rev. 114 (7) (2014) 3963–4038.
[11] S. Sen, P. Sarkar, Modelling of growth kinetics of isolated Pseudomonas sp. and optimization of parameters for enhancement of xanthine oxidoreductase production by Statistical Design of Experiments, J. Environm. Sci. Health, Part A 54 (1) (2019) 65–78.
[12] N. Ahmad, S. Sharma, V.N. Singh, S.F. Shamsi, A. Fatma, B.R. Mehta, Biosynthesis of Silver Nanoparticles from Desmodium triflorum: A Novel Approach Towards Weed Utilization, Biotechnol. Res. Int. 2011 (2011), 454090.
[13] R.G. Saratale, I. Karuppusamy, G.D. Saratale, A. Pugazhendhi, G. Kumar, Y. Park, G.S. Ghodake, R.N. Bharagava, J.R. Banu, H.S. Shin, A comprehensive review on green nanomaterials using biological systems: Recent perception and their future applications, Colloids Surf., B 170 (2018) 20–35.
[14] S. Ahmed, Annu, S. Ikram, S. Yudha, Biosynthesis of gold nanoparticles: A green approach, J. Photochem. Photobiol., B 161 (2016) 141–153.
[15] S.K. K, A. R, P. Arumugam, S. Berchmans, Synthesis of gold nanoparticles: an ecofriendly approach using Hansenula anomala, ACS Appl. Mater. Interfaces 3(5) (2011) 1418–25.
[16] T. Anukiruthika, S. Priyanka, J. Moses, C. Anandharamakrishnan, Characterisation of Green Nanomaterials, Springer, Green Nanomaterials, 2020, pp. 43–79.
[17] S. Sen, P. Sarkar, A novel third-generation xanthine biosensor with enzyme modified glassy carbon electrode using electrodeposited MWCNT and nanogold polymer composite film, RSC Adv. 5 (116) (2015) 95911–95925.
[18] K. Thandavan, S. Gandhi, S. Sethuraman, J.B.B. Rayappan, U.M. Krishnan, Development of electrochemical biosensor with nano-interface for xanthine sensing–a novel approach for fish freshness estimation, Food Chem 139 (1-4) (2013) 963–969.
[19] S. Çevik, Xanthine biosensor based on XO/AuNP/PtNP/MWCNT hybrid nanocomposite modified GCPE, Biotechnol. Bioprocess Eng. 21 (2) (2016) 314–320.
[20] R. Villalonga, P. Díez, M. Eguílaz, P. Martínez, J.M. Pingarrón, Supramolecular immobilization of xanthine oxidase on electropolymerized matrix of functionalized hybrid gold nanoparticles/single-walled carbon nanotubes for the preparation of electrochemical biosensors, ACS Appl. Mater. Interfaces 4 (8) (2012) 4312–4319.
[21] J. Zhao, M. Ma, X. Yan, D. Wan, Z. Zeng, P. Yu, D. Gong, Immobilization of lipase on β-cyclodextrin grafted and aminopropyl-functionalized chitosan/Fe3O4 magnetic nanocomposites: An innovative approach to fruity flavor esters esterification, Food Chem. 366 (2022), 130616.
[22] R. Devi, S. Yadav, C.S. Pundir, Au-colloids–polypyrrole nanocomposite film based xanthine biosensor, Colloids Surf., A 394 (2012) 38–45.
[23] S. Sadeghi, E. Fooladi, M. Malekaneh, A nanocomposite/crude extract enzyme-based xanthine biosensor, Anal. Biochem. 464 (2014) 51–59.
[24] B.Y. Sahyar, M. Kaplan, M. Ozsoz, E. Celik, S. Otles, Electrochemical xanthine detection by enzymatic method based on Ag doped ZnO nanoparticles by using polypyrrole, Bioelectrochemistry 130 (2019), 107327.
[25] M. Dervisevic, E. Custiuc, E. Çevik, Z. Durmus, M. Şenel, A. Durmus, Electrochemical biosensor based on REGO/Fe3O4 bionanocomposite interface for xanthine detection in fish sample, Food Control 57 (2015) 402–410.
[26] Y. Si, J.W. Park, S. Jung, G.-S. Hwang, E. Goh, H.J. Lee, Layer-by-layer electrochemical biosensors configuring xanthine oxidase and carbon nanotubes/graphene complexes for hypoxanthine and uric acid in human serum solutions, Biosens Bioelectron 121 (2018) 265–271.
[27] A. Bhattacherjee, T. Ghosh, A. Datta, Green synthesis and characterisation of antioxidant-tagged gold nanoparticle (X-GNP) and studies on its potent antimicrobial activity, J. Exp. Nanosci. 13 (1) (2018) 50–61.
[28] P. Pandey, S.P. Singh, S.K. Arya, V. Gupta, M. Datta, S. Singh, B.D. Malhotra, Application of Thiolated Gold Nanoparticles for the Enhancement of Glucose Oxidase Activity, Langmuir 23 (6) (2007) 3333–3337.
[29] S.M. Sreedharan, S.P. Singh, R. Singh, Flower Shaped Gold Nanoparticles: Biogenic Synthesis Strategies and Characterization, Indian J. Microbiol. 59 (3) (2019) 321–327.
[30] N. Wangoo, C.R. Suri, G. Shekhawat, Interaction of gold nanoparticles with protein: a spectroscopic study to monitor protein conformational changes, Appl. Phys. Lett. 92 (13) (2008), 133104.
[31] S. Roy, T.K. Das, Spectroscopic studies of interaction between biologically synthesized silver nanoparticles and bovine serum albumin, J. Nanosci. Nanotechnol. 14 (7) (2014) 4899–4905.
[32] T. Ghosh, P. Sarkar, A.P.F. Turner, A novel third generation uric acid biosensor using uricase electro-activated with ferrocene on a Nafion coated glassy carbon electrode, Bioelectrochemistry 102 (2015) 1–9.
[33] S.R. Saptarshi, A. Duschl, A.L. Lopata, Interaction of nanoparticles with proteins: relation to bio-reactivity of the nanoparticle, J. Nanobiotechnol. 11 (1) (2013) 1–12.
[34] J.D. Keighron, C.D. Keating, Enzyme: nanoparticle bioconjugates with two sequential enzymes: stoichiometry and activity of malate dehydrogenase and citrate synthase on Au nanoparticles, Langmuir 26 (24) (2010) 18992–19000.
[35] C.-S. Wu, C.-T. Wu, Y.-S. Yang, F.-H. Ko, An enzymatic kinetics investigation into the significantly enhanced activity of functionalized gold nanoparticles, Chem. Commun. 42 (2008) 5327, https://doi.org/10.1039/b810889g.
[36] S.N.J. Syed Zainol Abidin, N.H.N. Azman, S. Kulandaivalu, Y. Sulaiman, Poly(3,4-ethylenedioxythiophene) Doped with Carbon Materials for High-Performance Supercapacitor: A Comparison Study, J. Nanomater. 2017 (2017) 5798614.
[37] S. Kumar, M. Willander, J.G. Sharma, B.D. Malhotra, A solution processed carbon nanotube modified conducting paper sensor for cancer detection, J. Mater. Chem. B 3 (48) (2015) 9305–9314.
[38] Q. Zhao, R. Jamal, L. Zhang, M. Wang, T. Abdiryim, The structure and properties of PEDOT synthesized by template-free solution method, Nanoscale Res. Lett. 9 (1) (2014) 557.
[39] C. Peng, G.A. Snook, D.J. Fray, M.S.P. Shaffer, G.Z. Chen, Carbon nanotube stabilised emulsions for electrochemical synthesis of porous nanocomposite coatings of poly [3, 4-ethylene-dioxythiophene], Chem. Commun. 44 (2006) 4629, https://doi.org/10.1039/b609293d.
[40] A. Lakshmi, A. Raj, G. Gopu, P. Arumugam, C. Vedhi, Electrochemical, electrochromic behaviour and effects of supporting electrolyte on nano-thin film of poly 3, 4-ethylenedioxy thiophene, Electrochim. Acta 92 (2013) 452–459.
[41] X. Liu, X. Ou, Q. Lu, J. Zhang, S. Chen, S. Wei, Electrochemical sensor based on overoxidized dopamine polymer and 3, 4, 9, 10-perylenetetracarboxylic acid for simultaneous determination of ascorbic acid, dopamine, uric acid, xanthine and hypoxanthine, RSC Adv. 4 (80) (2014) 42632–42637.
[42] R.O. Olojo, R.H. Xia, J.J. Abramson, Spectrophotometric and fluorometric assay of superoxide ion using 4-chloro-7-nitrobenzo-2-oxa-1, 3-diazole, Anal. Biochem. 339 (2) (2005) 338–344.
[43] H. Ibrahim, Y. Temerk, A novel electrochemical sensor based on B doped CeO2 nanocubes modified glassy carbon microspheres paste electrode for individual and simultaneous determination of xanthine and hypoxanthine, Sens. Actuators, B 232 (2016) 125–137.
[44] J. Zhao, M. Ma, X. Yan, G. Zhang, J. Xia, G. Zeng, W. Tian, X. Bao, Z. Zeng, P. Yu, D. Gong, Expression and characterization of a novel lipase from Bacillus licheniformis NCU CS-5 for application in enhancing fatty acids flavor release for low-fat cheeses, Food Chem. 368 (2022), 130868.
[45] C. Lanzellotto, G. Favero, M. Antonelli, C. Tortolini, S. Cannistraro, E. Coppari, F. Mazzei, Nanostructured enzymatic biosensor based on fullerene and gold nanoparticles: Preparation, characterization and analytical applications, Biosens. Bioelectron. 55 (2014) 430–437.
[46] Y. Wen, J. Chang, L. Xu, X. Liao, L. Bai, Y. Lan, M. Li, Simultaneous analysis of uric acid, xanthine and hypoxanthine using voltammetric sensor based on nanocomposite of palygorskite and nitrogen doped graphene, J. Electroanal. Chem. 805 (2017) 159–170.
[47] N. Lavanya, C. Sekar, R. Murugan, G. Ravi, An ultrasensitive electrochemical sensor for simultaneous determination of xanthine, hypoxanthine and uric acid based on Co doped CeO2 nanoparticles, Mater. Sci. Eng., C 65 (2016) 278–286.
[48] Y. Wang, L.-L. Tong, Electrochemical sensor for simultaneous determination of uric acid, xanthine and hypoxanthine based on poly (bromocresol purple) modified glassy carbon electrode, Sens. Actuators, B 150 (1) (2010) 43–49.
[49] A.S. Kumar, P. Swetha, Ru (DMSO) 4Cl2 nano-aggregated Nafion membrane modified electrode for simultaneous electrochemical detection of hypoxanthine, xanthine and uric acid, J. Electroanal. Chem. 642 (2) (2010) 135–142.
[50] R. Ojani, A. Alinezhad, Z. Abedi, A highly sensitive electrochemical sensor for simultaneous detection of uric acid, xanthine and hypoxanthine based on poly (l-methionine) modified glassy carbon electrode, Sens. Actuators, B 188 (2013) 621–630.
[51] P.M.G. Ribeiro, H.S. Fernandes, L.B. Maia, S.F. Sousa, J.J.G. Moura, N.M.F.S. A. Cerqueira, The complete catalytic mechanism of xanthine oxidase: a computational study, Inorg. Chem. Front. 8 (2) (2021) 405–416.
[52] U. Batchu, K. Mandava, Biochemical role of xanthine oxidoreductase and its natural inhibitors: An overview, Int. J. Pharm. Pharm. Sci. 8 (10) (2016) 57–65.
[53] M.M. Rahman, H.M. Marwani, F.K. Algethami, A.M. Asiri, Xanthine sensor development based on ZnO–CNT, ZnO–CB, ZnO–GO and ZnO nanoparticles: an electrochemical approach, New J. Chemistry 41 (14) (2017) 6262–6271.
[54] M. Khan, M. Ahommed, M. Daizy, Detection of xanthine in food samples with an electrochemical biosensor based on PEDOT: PSS and functionalized gold nanoparticles, RSC Adv. 10 (59) (2020) 36147–36154.